

Attainable force volumes of optimal autonomous at-the-limit vehicle manoeuvres

Victor Fors, Björn Olofsson & Lars Nielsen

To cite this article: Victor Fors, Björn Olofsson & Lars Nielsen (2020) Attainable force volumes of optimal autonomous at-the-limit vehicle manoeuvres, *Vehicle System Dynamics*, 58:7, 1101-1122, DOI: [10.1080/00423114.2019.1608363](https://doi.org/10.1080/00423114.2019.1608363)

To link to this article: <https://doi.org/10.1080/00423114.2019.1608363>



© 2019 The Author(s). Published by Informa UK Limited, trading as Taylor & Francis Group



Published online: 22 Apr 2019.



Submit your article to this journal [↗](#)



Article views: 961





View related articles [↗](#)



View Crossmark data [↗](#)

Attainable force volumes of optimal autonomous at-the-limit vehicle manoeuvres

Victor Fors , Björn Olofsson  and Lars Nielsen

Division of Vehicular Systems, Department of Electrical Engineering, Linköping University, Linköping, Sweden

ABSTRACT

With new developments in sensor technology, a new generation of vehicle dynamics controllers is developing, where the braking and steering strategies use more information, e.g. knowledge of road borders. The basis for vehicle-safety systems is how the forces from tyre–road interaction is vectored to achieve optimal total force and moment on the vehicle. To study this, the concept of attainable forces previously proposed in literature is adopted, and here a new visualisation technique is devised. It combines the novel concept of attainable force volumes with an interpretation of how the optimal solution develops within this volume. A specific finding is that for lane-keeping it is important to maximise the force in a certain direction, rather than to control the direction of the force vector, even though these two strategies are equivalent for the friction-limited particle model previously used in some literature for lane-keeping control design. More specifically, it is shown that the optimal behaviour develops on the boundary surface of the attainable force volume. Applied to lane-keeping control, this observation indicates a set of control principles similar to those analytically obtained for friction-limited particle models in earlier research, but result in vehicle behaviour close to the globally optimal solution also for more complex models and scenarios.

ARTICLE HISTORY

Received 26 April 2018
Revised 12 February 2019
Accepted 3 April 2019

KEYWORDS

Active safety; force vectoring; vehicle dynamics control; tyre–road interaction; vehicle manoeuvre strategy

1. Introduction

Development of autonomous functions for vehicles is currently an active research area. This process includes the development of new active vehicle-safety systems, building on partial or full autonomy without human intervention. The main enablers for this promising development is more sensors installed in the vehicle and significantly increased onboard computing power. One main objective for achieving autonomy of the vehicle is situation awareness, and more specifically the ability for the vehicle to map the environment and have knowledge of the lane borders of the road for a certain look-ahead distance. This information can then be employed in the motion planning and control of the vehicle, in particular to the purpose of achieving optimal lane-keeping control [1,2]. Realisation of such control principles can give close to optimal performance, which has been described in, e.g. [3,4] (see further references on the subject in Section 1.1). Alternative approaches

CONTACT Victor Fors  victor.fors@liu.se

© 2019 The Author(s). Published by Informa UK Limited, trading as Taylor & Francis Group

This is an Open Access article distributed under the terms of the Creative Commons Attribution License (<http://creativecommons.org/licenses/by/4.0/>), which permits unrestricted use, distribution, and reproduction in any medium, provided the original work is properly cited.

compared to those presented in Section 1.1 when addressing mitigation and control for challenging manoeuvres are methods based on model predictive control (MPC) [5–7] and methods based on path tracking [8–10].

For the development of optimal lane-keeping control systems, it is critical to understand how the available tyre forces from interaction with the road can be used in the best possible way, given the information from the situation-awareness systems in the vehicle. This understanding is interesting from a number of perspectives, in particular to evaluate how close to optimal tyre utilisation a particular manoeuvre is, and perhaps more importantly, to devise new control strategies for optimal vehicle control in time-critical situations that are possible to realise for online execution.

With the perspectives indicated in the two previous paragraphs, we introduce a new visualisation technique based on the previously proposed concept of attainable forces [11]. It combines how the attainable forces develop over time with an optimal solution for a particular manoeuvre, resulting in a volume of attainable forces (see Section 4). The objective with this visualisation is to obtain insight from how the optimal manoeuvre develops within the attainable force volume. The information extracted from the plots of the attainable force volumes and an optimal solution can provide a basis for the development of strategies on how to vector the force and the moment on the vehicle. In the scenarios considered in this paper, it is observed that a local control approach for the given geometry and vehicle state, perhaps surprisingly, results in vehicle behaviour close to the globally optimal solution. This observation is important, since it indicates a set of control strategies that can be implemented and executed online.

1.1. Background

Analytical solutions of optimal control problems related to safety-critical manoeuvres exist for certain models and scenarios. In [3], a control law referred to as the parabolic path reference strategy (PPR) was proposed. The PPR strategy is based on optimal control of a friction-limited particle model and was shown to result in good performance compared to conventional yaw control. The PPR strategy was integrated and developed into a complete control design in [4], which is able to account for nonlinear models of the tyre forces. In [12], the solution from optimal control of a friction-limited particle model was used for lane-change control.

To find optimal solutions for problems that are analytically intractable to solve, numerical optimal control techniques can be used. By the use of numerical optimal control, the maximum initial velocity that can be handled in a left-hand turn was examined in [1], showing that braking to reduce speed was given priority over braking to contribute to a turn-in yaw moment. A continuous family of braking patterns was found in [2], by using a weighted cost function of initial and final velocity. There, significant similarities in the optimal trajectories were found between different safety-critical scenarios. In [13], different actuator configurations of a vehicle were examined using numerical optimal control for the same scenarios as in the current paper. It was noted that in the trade-off between reducing speed and cornering, full braking is initially required at the expense of the steering ability. Torque vectoring for minimum-time cornering was examined in [14] by using optimal steering inputs given by numerical optimal control. It was demonstrated that the performance of a vehicle capable of

torque vectoring is largely insensitive to the uncontrolled understeer behaviour of the vehicle.

One interesting perspective with numerical optimal control is to find general characteristics in the obtained solutions, which can be used in future control systems. In [11], attainable forces from applying wheel forces were computed at selected time instants of a manoeuvre to evaluate the potential of different actuator configurations in vehicles. The results visualised, when compared with individual wheel drive, that there was less potential to contribute to the turn-in yaw moment with individual wheel brakes only. Numerical optimal control was used in [15] to investigate mitigation of secondary collisions post impact. By examining the attainable forces in optimal manoeuvres, the trade-off between yaw-moment control and lateral force control was examined. From the findings in [15], a subsequent control design was presented in [16]. Plots of the attainable forces were used to evaluate the similarity of the closed-loop control compared to the optimal solution. The papers [17,18] extend the results from [15,16] by also considering front-axle steering control in addition to individual braking, to minimise the lateral deviation. Attainable forces can thus be a powerful tool in the search for new control principles when analysing numerical solutions.

The research cited in the previous paragraphs demonstrate the feasibility of finding inspiration for new control principles based on optimal control. In particular, it is interesting to investigate if strategies similar to those analytically obtained for friction-limited particle models in certain scenarios can be found for more complex vehicle models and scenarios. The scenario considered in [15–18] can be interpreted as a particular case of lane-keeping control, i.e. staying on a straight road under challenging initial conditions. This is encouraging for the use of attainable forces to analyse other manoeuvres related to lane keeping.

2. Scenarios

Two common safety-critical scenarios are used in this paper to illustrate the developed method. The first scenario is a left-hand turn with constant curvature. The second scenario is a double lane-change based on the ISO standard 3888-2 [19]. To simplify the constraints introduced by the scenarios, only one point in the volume spanned by the vehicle is considered in the path constraints, rather than ensuring that no part of the vehicle volume violates any constraints.

2.1. Left-hand turn scenario

The left-hand turn scenario is illustrated in Figure 1, where the vehicle enters the turn at the centre of the lane from the left-hand side. For the optimal control problem (OCP) to be solved in Section 3.2, the initial state of the vehicle is set to the position and orientation marked by OCP start in Figure 1. The manoeuvre is considered to end at the time t_f when the deviation from the centre of the lane, denoted e , stops increasing, i.e. when $\dot{e}(t_f) \leq 0$. The turn has a radius of 30 m and the vehicle position (X_p, Y_p) is constrained by a maximum deviation from the centre of the lane, $|e| \leq d$, where d is the half width of the lane that is chosen as 1 m.

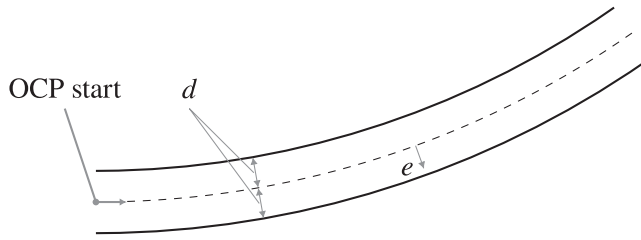


Figure 1. Illustration of the left-hand turn scenario. The dashed line marks the centre of the lane and the black curves mark the borders for the vehicle position (X_p, Y_p) .

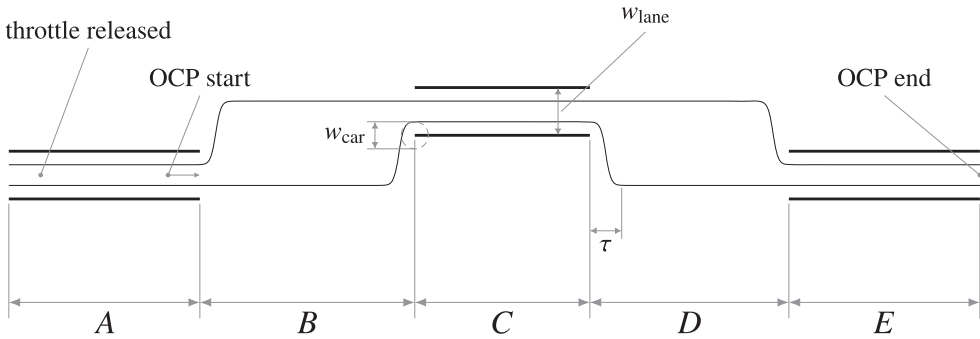


Figure 2. Illustration of the double lane-change track. The black bars mark the placement of the cones according to the ISO standard 3888-2 and the black curves mark the borders for the vehicle position (X_p, Y_p) .

2.2. Double lane-change scenario

The double lane-change scenario is illustrated in Figure 2. The numerical track parameters used are chosen based on the ISO standard 3888-2 [19]; the parameters are collected in Table 1. The starting position of the vehicle is selected to be centred in the lane and 10 m from the left-hand side of the track. Since only the vehicle position (X_p, Y_p) is constrained, the boundaries are made more narrow than the cone placement specified by the standard to compensate for the vehicle width. Mathematically, the track is modelled using top and bottom lane constraints according to

$$Y_p \leq Y_t(X_p) = a + c(H(X_p - X_{t1}) - H(X_p - X_{t2})), \tag{1}$$

$$Y_p \geq Y_b(X_p) = -a + c(H(X_p - X_{b1}) - H(X_p - X_{b2})), \tag{2}$$

$$H(x) = 0.5 \left(1 + \tanh \left(\frac{2\pi x}{\tau} \right) \right), \tag{3}$$

where H is a sigmoid function and $a, c, X_{t1}, X_{t2}, X_{b1}, X_{b2}$, and τ are numerical parameters defined in Table 1.

Table 1. Parameters used for the double lane-change track. All of the parameter units are in metres.

Notation	Value (m)
A	12
B	13.5
C	11
D	12.5
E	12
w_{lane}	3
w_{car}	1.7
τ	2
a	$(w_{\text{lane}} - w_{\text{car}})/2$
c	$w_{\text{lane}} + 1$
X_{r1}	$A + \tau/2$
X_{r2}	$A + B + C + D - \tau/2$
X_{b1}	$A + B - \tau/2$
X_{b2}	$A + B + C + \tau/2$

3. Modelling and optimisation

This section provides a description of the adopted vehicle model and the optimisation approach employed for computing the optimal manoeuvres to be analysed using attainable force volumes.

3.1. Vehicle model

The vehicle model is a double-track model (see Figure 3), with longitudinal and lateral load transfer between the different wheels included. A nonlinear tyre model based on Pacejka's Magic Formula [20] is employed, and weighting functions as suggested in [20] are used for describing the tyre forces under combined longitudinal and lateral tyre slip. In the employed tyre model with parameters originating from [20], the tyre forces scale linearly with the normal force acting on the tyre, which is a simplification of the actual tyre characteristics but is considered justified based on previous tyre-model investigations in the context of optimisation [21]. The vehicle is moving in a globally fixed coordinate system, defined by the position (X_p, Y_p) , marking the vehicle centre of rotation in the vehicle frame, and the heading angle ψ (see Figure 3). The inputs to the model are the steering angle δ and the commanded wheel torques $T_{u,i}$, $i = 1, 2, 3, 4$, each acting on the applied wheel torque T_i for the corresponding wheel through a first-order system. For the torques, $T_{u,i}$, only braking is considered, i.e. no positive commanded torques, and the time constant of the braking system is selected as 0.1 s. The highest allowed commanded braking torques are selected as $T_{u,i,\min} = -\mu_{x,i}mgR_w$, where $\mu_{x,i}$ is the longitudinal friction coefficient of tyre i , m is the vehicle mass, g is the gravitational acceleration constant, and R_w is the wheel radius. The steering angle and steering rate are limited to $\delta_{\max} = 0.5$ rad and $\dot{\delta}_{\max} = 1$ rad/s, respectively. A summary of the inputs to the model and the vehicle states is given in Table 2. The model equations and model parameters are specified in [21], where the model employed in this paper is referred to as DT-WF.

3.2. Optimal control problem

The problem of finding optimal steering and braking sequences is stated as finding the solution to an optimal control problem (OCP). The approach from [2] is adopted, where a

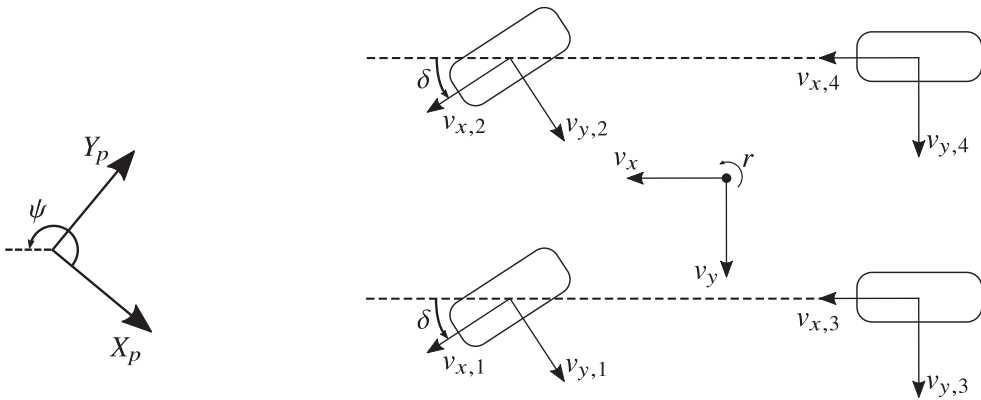


Figure 3. Double-track vehicle model and its associated global coordinate system.

Table 2. Vehicle states and inputs in the adopted double-track model with a nonlinear tyre-friction model.

Description	Notation
Position and orientation	X_p, Y_p, ψ
Velocity and yaw rate	v_x, v_y, r
Roll and pitch motion	$\phi, \dot{\phi}, \theta, \dot{\theta}$
Steer angle	δ
Rotational wheel speeds	$\omega_1, \omega_2, \omega_3, \omega_4$
Wheel slip angles	$\alpha_1, \alpha_2, \alpha_3, \alpha_4$
Applied wheel torques	T_1, T_2, T_3, T_4
Commanded wheel torques	$T_{u,1}, T_{u,2}, T_{u,3}, T_{u,4}$

continuous family of optimal braking patterns in autonomous manoeuvres was presented. More specifically, an optimisation criterion to be minimised, with a weighted combination of the initial velocity v_0 and the final velocity v_f of the manoeuvre, was introduced according to

$$J = -\eta v_0 - (1 - \eta)v_f, \quad 0 \leq \eta \leq 1. \tag{4}$$

The intuition behind this formulation is that in order to stay in lane, all-wheel braking is typically performed when at the maximum entry speed possible to handle, whereas if the entry speed is below the maximum, it can be advantageous to not brake more than necessary, which can be formulated as maximising the exit speed (see [2] for further motivation and discussion). The OCP includes constraints on the control inputs u , i.e. the wheel torques $T_{u,i}$ and the steering angle δ . In addition, the path constraints introduced for the scenarios in Section 2 are represented by the function f . Mathematically, the OCP is stated over the time interval $[t_0, t_f]$ as follows (where the final time t_f is unknown a priori):

$$\text{minimise } J, \tag{5a}$$

$$\text{subject to } T_{u,i,\min} \leq T_{u,i} \leq 0, \quad i \in \{1, 2, 3, 4\}, \tag{5b}$$

$$|\delta| \leq \delta_{\max}, \quad |\dot{\delta}| \leq \dot{\delta}_{\max}, \quad f(X_p, Y_p) \leq 0, \tag{5c}$$

$$F_c x(0) = \tilde{x}_0, \quad G_c x(t_f) = \tilde{x}_f, \quad g(x(t_f)) \leq 0, \tag{5d}$$

$$\dot{x} = G(x, z, u), \quad h(x, z, u) = 0. \tag{5e}$$

The matrices F_c and G_c specify the states where initial and terminal constraints are enforced (denoted with \tilde{x}_0 and \tilde{x}_f , respectively). Further, the function g specifies possible terminal inequality constraints on the states. The functions G and h define the vehicle dynamics with the dynamic state vector x , algebraic variable vector z , and input vector u . In the optimal manoeuvres computed in this paper, the OCP is solved for the optimisation criterion given by extreme points of (4), i.e. $\eta = 1$ or $\eta = 0$. This implies that J is chosen as either $J = -v_0$ or $J = -v_f$. As illustrated in [2], these two cases correspond to optimal lane keeping and optimal yaw control, respectively. The intuition behind these interpretations is that maximum entry speed corresponds to optimal lane keeping, whereas optimising exit speed turns out to avoid braking on the outer wheels, i.e. only braking of the inner wheels is performed, similar to traditional yaw control (see Figure 5 in Section 5).

The resulting optimisation problem is solved numerically using the JModelica.org simulation and optimisation platform [22] with the methodology presented in [21]. The numerical method for solving the continuous-time optimisation problem (5) is based on direct collocation [23]. The collocation procedure handled by JModelica.org results in a large nonlinear optimisation program, where the optimisation variables correspond to the interpolation values of the collocation polynomials at the collocation points for the trajectories of the inputs, states, and algebraic variables of the model. In the solution of the resulting nonlinear program, IPOPT [24] with the linear solver HSL MA57 [25] is used. In JModelica.org, the CasADi tool [26] is used for computing the necessary Jacobians and Hessians using algorithmic differentiation.

4. Forces

The resulting forces on the vehicle from the employed actuation in an at-the-limit manoeuvre are of particular importance to study. Forces acting in certain globally fixed directions during an optimal manoeuvre can give intuition for control design, and a close investigation of the computed optimal manoeuvres is thus beneficial for design of future functions for vehicle safety and autonomy. In this section, the tools used for analysing and visualising the behaviour of vehicle manoeuvres are defined. Firstly, forces of interest for the scenarios considered in this paper are defined. Secondly, the procedure used here for computing attainable forces is defined. Finally, a new visualisation of the attainable forces is introduced.

4.1. Global forces

In [15], the optimisation criterion was to minimise the deviation from the straight centreline of a road during a vehicle manoeuvre, and in that paper the force acting in the direction that opposes the path deviation was noted to be of particular interest. Moreover, in [3] an analytical solution of an optimal control problem to minimise the maximum deviation from the centreline of the road during a left-hand turn scenario was derived for a friction-limited particle model of the vehicle. The particular globally fixed force vector that was found to contribute to lane keeping was later used for designing a controller for vehicle stabilisation [4]. Also in [3], it was noted that for optimal control of a double-track vehicle model in a left-hand turn, the direction of the acceleration vector in globally fixed coordinates is largely constant during the manoeuvre. Further, related analytical solutions of

an optimal control problem have been derived for friction-limited particle models in [27] in single-obstacle avoidance scenarios. These observations and control designs in previous research motivate the interest for certain global forces on the vehicle arising during manoeuvring scenarios.

4.1.1. Control force vector

In a lane-keeping scenario, the force lateral with respect to the road can be more important to control in order to reduce the lateral error of the vehicle than the lateral force with respect to the vehicle ego orientation. For at-the-limit manoeuvres where the focus is to avoid driving off the road or crash into another vehicle rather than staying close to the centre of the lane, forces that are especially important to control can analogously be found. The force vector that includes the components important for control purposes is here named the control force vector F_c and is theoretically justified in Section 4.1.2. In order to make an analysis of global forces of interest for the scenarios considered in this paper (see Section 2), it is for a single turn assumed that t_f is the time when the vehicle stabilises – i.e. the vehicle no longer decreases its distance to the most immediate obstacle. The particular global force component of interest, in this paper denoted $F_{c,y}$, is then acting in a globally fixed direction that points into the curve and perpendicular to the direction of the final velocity vector ψ_v . Also the global force acting in the direction of the final velocity vector is of interest; this force is here named $F_{c,x}$. Intuitively, $F_{c,y}$ is the force that stops the approach of the vehicle toward the obstacle whereas $F_{c,x}$ influences the final velocity. For further reference and clarity, some key concepts and notations in this paper are introduced as definitions. The first definition concerns the selected global forces of interest.

Definition 4.1 (Control force vector F_c): The components of the control force vector F_c , $F_{c,x}$ and $F_{c,y}$, are acting in the directions of interest for lane-keeping control as illustrated in Figure 4. Expressed in terms of the forces $F_{p,x}$ and $F_{p,y}$ in the globally fixed coordinate system, or in terms of the local vehicle longitudinal and lateral forces, F_x and F_y , the control forces $F_{c,x}$ and $F_{c,y}$ are calculated according to the expression

$$\begin{bmatrix} F_{c,x}(t) \\ (-1)^n F_{c,y}(t) \end{bmatrix} = \begin{bmatrix} \cos(\psi_v(t_f)) & \sin(\psi_v(t_f)) \\ -\sin(\psi_v(t_f)) & \cos(\psi_v(t_f)) \end{bmatrix} \begin{bmatrix} F_{p,x}(t) \\ F_{p,y}(t) \end{bmatrix} \quad (6)$$

$$= \begin{bmatrix} \cos(\psi_v(t_f)) & \sin(\psi_v(t_f)) \\ -\sin(\psi_v(t_f)) & \cos(\psi_v(t_f)) \end{bmatrix} \begin{bmatrix} \cos(\psi(t)) & -\sin(\psi(t)) \\ \sin(\psi(t)) & \cos(\psi(t)) \end{bmatrix} \begin{bmatrix} F_x(t) \\ F_y(t) \end{bmatrix}, \quad (7)$$

where t_f is the time when the vehicle no longer decreases its distance to the obstacle, ψ_v is the angle defining the direction of the velocity vector, and n is 0 for a left-hand turn and 1 for a right-hand turn. ■

For more complex manoeuvres than a single turn, different definitions of F_c could be made along the path to mirror the varying road geometry. This generalisation of Definition 4.1 is illustrated in Figure 4. Note that in the general case, the angle $\psi_v(t_f)$ is unknown a priori. This angle is known in hindsight, after the OCPs for the particular scenarios have been solved. This fact does not imply any limitation for the offline evaluation in this paper.

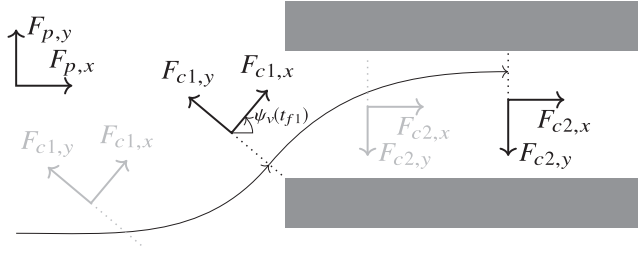


Figure 4. Geometric description of the control forces $F_{c,x}$ and $F_{c,y}$ in Definition 4.1 in an example scenario. The curved line describes the vehicle path with arrowheads where the individual turns end. The variable ψ_v defines the angle between the x -component of the global force, $F_{p,x}$, and the velocity vector. Note that the angle of the final velocity vector is $\psi_v(t_{f2}) = 0$ in the above scenario.

4.1.2. Motivation of control force vector by analytical optimal control

For friction-limited particle models, analytical solutions of OCPs can be found for a number of different scenarios, see, e.g. [3,12,27,28]. While analytical solutions to the OCP (5) are intractable, an approximate partial solution can be analytically derived to motivate the control force vector in Definition 4.1. This intuitive derivation is done by using Pontryagin's maximum principle [29] with the same methodology as used for a friction-limited particle model in [3], but for a more general model and scenario. For simplicity, the vehicle states in Table 2 are reduced to the vehicle position and orientation (defined in globally fixed coordinates) and their time derivatives according to

$$x = [X_p, Y_p, \psi, \dot{X}_p, \dot{Y}_p, \dot{\psi}]^T. \quad (8)$$

To simplify further, it is assumed that the available vehicle forces and moment are primarily affected by the vehicle orientation. The system dynamics can then be modelled as the first-order ordinary differential equation

$$\dot{x} = f(x, u) = [\dot{X}_p, \dot{Y}_p, \dot{\psi}, F_{p,x}(\psi, u)/m, F_{p,y}(\psi, u)/m, M_z(\psi, u)/I_{zz}]^T, \quad (9)$$

where u is the constrained system input, $F_{p,x}(\psi, u)$ and $F_{p,y}(\psi, u)$ are the vehicle forces in the globally fixed coordinate system, m the vehicle mass, $M_z(\psi, u)$ the yaw moment, and I_{zz} the moment of inertia about the z -axis. For optimal control with focus on lane-keeping or avoiding obstacles, the terminal objective that represents fulfilling all obstacle or lane constraints is

$$\text{maximise } J = \text{maximise } \frac{1}{2} (\Delta X^2(t_f) + \Delta Y^2(t_f)), \quad (10)$$

where ΔX and ΔY are the distances from the obstacle along the X_p and Y_p axes, respectively, where the obstacle could be the lane border of the road. If the obstacle constraints are not fulfilled, the value of J is zero and otherwise positive. The final time t_f is when the vehicle stops approaching the obstacle as per Definition 4.1 – i.e. the distance and velocity vectors are orthogonal – resulting in the terminal constraint

$$\Delta X(t_f)\dot{X}_p(t_f) + \Delta Y(t_f)\dot{Y}_p(t_f) = 0. \quad (11)$$

To solve (10), the system dynamics (9) are extended with the co-states $\lambda(t)$ to the Hamiltonian

$$H(x, u, \lambda) = \lambda^T f = \lambda_1 \dot{X}_p + \lambda_2 \dot{Y}_p + \lambda_3 \dot{\psi} + \frac{\lambda_4}{m} F_{p,x}(\psi, u) + \frac{\lambda_5}{m} F_{p,y}(\psi, u) + \frac{\lambda_6}{I_{zz}} M_z(\psi, u). \tag{12}$$

For optimality for an arbitrary t_f , the following relations have to be satisfied [30]:

$$\max_u H(x^*(t), u, \lambda(t)) = H(x^*(t), u^*(t), \lambda(t)) = H^*, \quad 0 \leq t \leq t_f, \tag{13}$$

$$\dot{\lambda}(t) = -\frac{\partial H^*}{\partial x}, \tag{14}$$

$$\lambda(t_f) = \left. \frac{\partial J}{\partial x} \right|_{t=t_f}. \tag{15}$$

The relation (13) gives for the Hamiltonian (12) that the optimal Hamiltonian H^* and the optimal input u^* are given by

$$\begin{aligned} H^* &= \max_u \left(\underbrace{\lambda_1 \dot{X}_p + \lambda_2 \dot{Y}_p + \lambda_3 \dot{\psi}}_{H_0(x,\lambda)} + \underbrace{\frac{\lambda_4}{m} F_{p,x}(\psi, u) + \frac{\lambda_5}{m} F_{p,y}(\psi, u) + \frac{\lambda_6}{I_{zz}} M_z(\psi, u)}_{H_1(x,u,\lambda)} \right) \\ &= \max_u H_1(x^*, u, \lambda) + H_0(x^*, \lambda), \end{aligned} \tag{16}$$

$$u^* = \arg \max_u H_1(x^*, u, \lambda), \tag{17}$$

where $H_0(x, \lambda)$ is the part of the Hamiltonian independent of the input u and $H_1(x, u, \lambda)$ is the part of the Hamiltonian dependent on the input u . Since $F_{p,x}$, $F_{p,y}$, and M_z appear linearly in H_1 , the optimal input u^* should be selected such that the linear combination of the available forces and moment maximises H_1 . If the system is over-actuated such that the available forces and moment form a volume, this observation implies that the optimal solution is on the boundary surface of this volume (see [16]). The conditions (14) and (15) are used to find an expression for λ . The terminal value for λ is computed from (15), which gives

$$\lambda(t_f) = [\Delta X(t_f), \Delta Y(t_f), 0, 0, 0, 0]^T. \tag{18}$$

The co-state dynamics are computed from (14) and are integrated as follows:

$$\dot{\lambda} = \left[0, 0, -\frac{\partial H_1}{\partial \psi}, -\lambda_1, -\lambda_2, -\lambda_3 \right]^T, \tag{19}$$

$$\begin{aligned} \lambda &= \left[C_1, C_2, -\int \frac{\partial H_1}{\partial \psi} dt, -\int \lambda_1 dt, -\int \lambda_2 dt, -\int \lambda_3 dt \right]^T \\ &= \left[C_1, C_2, -\int \frac{\partial H_1}{\partial \psi} dt, C_3 - C_1 t, C_4 - C_2 t, \int \left(\int \frac{\partial H_1}{\partial \psi} dt \right) dt \right]^T, \end{aligned} \tag{20}$$

where C_i are integration constants. In (16)–(17), it is seen that to find an expression for the optimal input u^* , only the co-states λ_4 , λ_5 , and λ_6 are of interest. Inserting the terminal values from (18) to find the integration constants gives

$$\lambda_4 = (t_f - t) \Delta X(t_f), \tag{21}$$

$$\lambda_5 = (t_f - t)\Delta Y(t_f), \quad (22)$$

$$\lambda_6 = \int_t^{t_f} \left(\int_{t'}^{t_f} \frac{\partial H_1(x(t''), u(t''), \lambda(t''))}{\partial \psi} dt'' \right) dt', \quad (23)$$

where it is observed that the ratio between the co-states λ_4 and λ_5 is constant and that λ_6 depends on how much future H_1 can be increased by changing the orientation ψ . The optimal input is now more explicitly written by substituting the expressions for λ_4 and λ_5 into (17), which gives

$$u^* = \arg \max_u \left(\frac{(t_f - t)}{m} (\Delta X(t_f)F_{p,x} + \Delta Y(t_f)F_{p,y}) + \frac{\lambda_6}{I_{zz}}M_z \right). \quad (24)$$

To get closer to expression (6) in Definition 4.1 the ratio between the forces $F_{p,x}$ and $F_{p,y}$ should be expressed in terms of the final velocity vector $\psi_v(t_f)$. Assuming that t_f fulfills the terminal constraint (11), the distance vector from the obstacle at time t_f can be rewritten in terms of the angle of the velocity vector $\psi_v(t_f)$ according to

$$\begin{aligned} \begin{bmatrix} \Delta X(t_f) \\ \Delta Y(t_f) \end{bmatrix} &= \sqrt{\Delta X^2(t_f) + \Delta Y^2(t_f)} \begin{bmatrix} \cos(\psi_v(t_f) + (-1)^n \pi/2) \\ \sin(\psi_v(t_f) + (-1)^n \pi/2) \end{bmatrix} \\ &= \sqrt{\Delta X^2(t_f) + \Delta Y^2(t_f)} \begin{bmatrix} -(-1)^n \sin(\psi_v(t_f)) \\ (-1)^n \cos(\psi_v(t_f)) \end{bmatrix}, \end{aligned} \quad (25)$$

where n is 0 or 1 depending on the direction of the turn, see Definition 4.1. Using the expression for $F_{c,y}$ given by (6) in Definition 4.1, the optimal input (24) can be expressed as

$$\begin{aligned} u^* &= \arg \max_u \left(\frac{(t_f - t)\sqrt{\Delta X^2(t_f) + \Delta Y^2(t_f)}}{m} \begin{bmatrix} -(-1)^n \sin(\psi_v(t_f)) \\ (-1)^n \cos(\psi_v(t_f)) \end{bmatrix}^T \begin{bmatrix} F_{p,x} \\ F_{p,y} \end{bmatrix} + \frac{\lambda_6}{I_{zz}}M_z \right) \\ &= \arg \max_u \left(\frac{(t_f - t)\sqrt{\Delta X^2(t_f) + \Delta Y^2(t_f)}}{m} F_{c,y} + \frac{\lambda_6}{I_{zz}}M_z \right). \end{aligned} \quad (26)$$

The optimal input u^* should thus be selected such that the linear combination of $F_{c,y}$ and M_z maximises H_1 . If the available $F_{c,y}$ and M_z form a surface, the optimal solution should at each time instant be on its boundary. Additionally, since the term multiplied with $F_{c,y}$ is always positive, the optimal solution is always on the side of this surface where $F_{c,y}$ is larger. The same conclusions hold true if the vehicle forces and moment in (9) are also dependent on the yaw rate $\dot{\psi}$.

4.2. Attainable forces from individual braking

It is of interest to study when, or if, creating a yaw moment M_z about the vehicle z -axis is given priority over momentarily maximising the control forces $F_{c,x}$ or $F_{c,y}$ (defined in Definition 4.1) during the studied manoeuvres. Further, it is illustrative to study how priority of $F_{c,x}$ influences $F_{c,y}$, and vice versa. A further quantity of interest is the contribution

ΔM to the total yaw moment M_z from the individual braking forces on each wheel. This quantity is defined, equivalently to in [1], as follows.

Definition 4.2 (Yaw-moment contribution ΔM from braking): For each wheel $i \in \{1, 2, 3, 4\}$, the expression for ΔM_i is

$$\Delta M_i = \begin{bmatrix} l_{x,i} & l_{y,i} \end{bmatrix} \begin{bmatrix} F_{x,i} \sin(\delta_i) + (F_{y,i} - F_{y0,i}) \cos(\delta_i) \\ (F_{y,i} - F_{y0,i}) \sin(\delta_i) - F_{x,i} \cos(\delta_i) \end{bmatrix}, \quad (27)$$

where $l_{x,i}$ and $l_{y,i}$ are the longitudinal and the lateral distance from the centre of rotation in the vehicle frame to wheel i , respectively, $F_{x,i}$ and $F_{y,i}$ are the longitudinal and the lateral force on wheel i , respectively, and $F_{y0,i}$ is the nominal lateral force on wheel i in the absence of braking. The total yaw-moment contribution is then given by

$$\Delta M = \sum_{i=1}^4 \Delta M_i. \quad (28)$$

■

As proposed and employed in [11], the combination of the force and yaw moment at a particular time instant during a computed vehicle manoeuvre can be plotted together with all the possible momentarily attainable forces (arising for different combinations of individual actuator actions), see Figure 6 for an example. The term *attainable forces* from [11,15–18] in this context refers to the global force and yaw moment that can be obtained by variations of the tyre forces, under the assumption that the vehicle states affecting the tyre forces can instantaneously change. The plot concept presented in those papers is in this paper extended in two different directions. Firstly, the forces $F_{c,x}$ and $F_{c,y}$, which act in directions dependent on the optimal manoeuvring path and trajectory, are used in the plots to compare with the yaw moment ΔM . Secondly, three-dimensional plots of the attainable force volume are introduced, see Section 4.3.

4.2.1. Computing attainable forces from individual braking

As in [11], an approximation of the attainable forces arising from different degrees of individual braking from all four wheels is created with a computational method that explores combinations of contributions from the individual tyre forces. As in [15], the attainable forces are computed for selected time instants during optimal manoeuvres. Out of the vehicle states and inputs in Table 2, the wheel speed ω_i for each wheel $i \in \{1, 2, 3, 4\}$ is made to change instantaneously to compute attainable forces from individual braking. The other states and inputs, e.g. the steering angle δ and the slip angle α_i , are given by their original values, i.e. the solution to the OCP (5). Changing the wheel speed ω_i influences the slip ratio κ_i for each wheel i , and thus also influences the longitudinal and lateral tyre forces.

The attainable forces are computed according to the following definition.

Definition 4.3 (Attainable forces): To compute the attainable forces at a particular time instant t , the longitudinal slip κ_i for each wheel $i \in \{1, 2, 3, 4\}$ is changed to different values in the interval $\kappa_i = [\kappa_{\min}, \dots, \kappa_{\max}]$. The slip interval is discretised using a grid with N points. For each of the different combinations of wheel slips, certain wheel forces, and thus

global vehicle forces, are obtained. The set of the so obtained vehicle forces defines the attainable forces at time instant t . ■

The longitudinal slip κ_i for each wheel is discretised in the plots presented in Sections 6–7 using $N = 30$ points. The maximum κ is set to $\kappa_{\max} = 0$, since with no driving-wheel moment the maximum possible value of κ is close to zero. A minimum κ of $\kappa_{\min} = -0.3$ is used, which is enough for the tyre parameters used to include the interesting regions of the force–slip curve. An approximation of the attainable forces resulting from different degrees of individual braking from all four wheels can thus be created by combinations of the individual tyre forces, yielding in total 30^4 discrete combinations for the considered forces and yaw moment.

4.3. Attainable force volumes

The attainable forces, as defined in Definition 4.3, change over time during a vehicle manoeuvre. To visualise this, the concept of attainable force volumes and their boundaries are defined.

Definition 4.4 (Attainable force volume): The boundary of the attainable forces as defined in Definition 4.3 is computed at different instants of time t during the manoeuvre and are subsequently connected, thus forming a three-dimensional surface. This surface is denoted $\partial\mathcal{F}$. The corresponding volume enclosed by $\partial\mathcal{F}$ and the endpoints of the time interval t is denoted \mathcal{F} . The volume \mathcal{F} can be illustrated using different global forces and yaw moments; this dependency is indicated with the notation $\mathcal{F}(\cdot, \cdot)$. ■

In light of the defined control forces $F_{c,x}$ and $F_{c,y}$ given by (7) in Definition 4.1, and the yaw moment ΔM given by (28) in Definition 4.2, two different illustrations of the attainable force volumes are considered in this paper. These volumes are denoted $\mathcal{F}(\Delta M, F_{c,x})$ and $\mathcal{F}(\Delta M, F_{c,y})$, respectively.

5. Control forces during the left-hand turn

This section analyses the trajectories of the control forces defined in Section 4.1, retrieved by solving the OCP (5). For an analysis of the corresponding individual resulting state trajectories obtained by solving the OCP, the reader is referred to [2]. As mentioned in Section 3.2, optimal lane-keeping control and optimal yaw control are embedded as the boundary values of (4), corresponding to the optimisation criteria $J = -v_0$ and $J = -v_f$, respectively. The optimal lane-keeping solutions ($J = -v_0$) were shown to brake all four wheels to reduce the vehicle velocity, while the optimal yaw control solutions ($J = -v_f$) were shown to brake only the wheels on one side of the vehicle for additional turn-in yaw moment. In Figure 5, the trajectories of the control forces $F_{c,y}$ and $F_{c,x}$ are shown together with the steering angle δ , the wheel torques T_i , $i = 1, 2, 3, 4$, and the moment ΔM resulting from the braking forces. The orientations of the control force vector F_c in the solutions obtained for the two optimisation criteria differ, since the manoeuvres have different final velocity vectors $\psi_v(t_f)$.

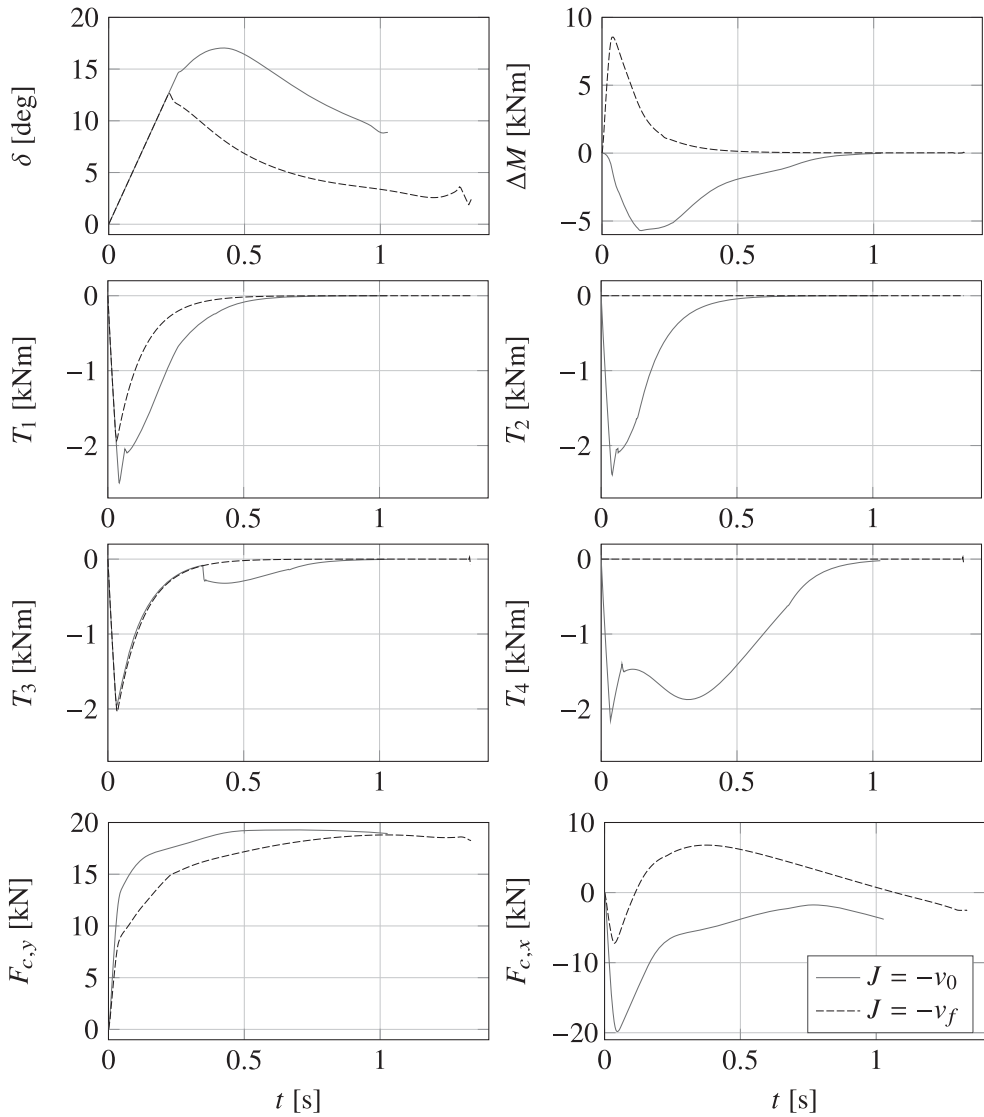


Figure 5. Optimal trajectories for different optimisation criteria during the left-hand turn scenario: δ , steering angle; ΔM , moment resulting from braking torques; T_1 , applied wheel torque on the front-left wheel; T_2 , applied wheel torque on the front-right wheel; T_3 , applied wheel torque on the rear-left wheel; T_4 , applied wheel torque on the rear-right wheel; $F_{c,y}$, y -component of the control force vector (Definition 4.1); $F_{c,x}$, x -component of the control force vector (Definition 4.1).

There are several interesting aspects to point out in the results shown in Figure 5. The steering angle can be seen to be limited by a steering-rate constraint at the beginning of the manoeuvre for both solutions. Differences in actuation between the two solutions are thus initially only in terms of braking. The solution for $J = -v_0$ utilises four-wheel braking, whereas $J = -v_f$ results in braking torques only on the inner wheels. It is seen that the value of $F_{c,y}$ is comparably greater for $J = -v_0$ than for $J = -v_f$ for most of the manoeuvre, whereas the value of $F_{c,x}$ is comparably greater for $J =$

$-v_f$ than for $J = -v_0$. These results are intuitive considering the difference in optimisation criteria. Perhaps not as intuitive is the moment ΔM resulting from braking for the optimisation criterion $J = -v_0$. Here, the moment ΔM contributes to the total moment with a turn-out moment, whereas for the optimisation criterion $J = -v_f$, the moment ΔM is a turn-in moment instead. The reason for this behaviour is explained in Section 7.1.2.

6. Attainable forces during the left-hand turn

In this section, the left-hand turn scenario is analysed with respect to the attainable forces as defined by Definition 4.3 in Section 4.2. The attainable forces are illustrated with two-dimensional cloud plots in Figure 6, employing the plot style proposed in [11]. Figure 6 shows the attainable $F_{c,y}$ and ΔM for the left-hand turn scenario with $J = -v_0$ at different time instants in two-dimensional plots. The optimal solution is marked in the gray cloud of attainable forces as a black filled circle. In the beginning of the manoeuvre, the attainable forces are almost shaped like a diamond. During this part of the manoeuvre, the interpretation of the different parts of the diamond is as follows. The bottom corner corresponds to no braking, the top corner corresponds to close to maximum braking forces, the left corner corresponds to maximum braking forces on the right wheels, and the right corner corresponds to maximum braking forces on the left wheels. Considering the vehicle path schematically illustrated in Figure 4, the vector corresponding to the control force $F_{c,y}$ will eventually be orthogonal to the velocity vector of the vehicle and the vehicle orientation, and the possibility to increase $F_{c,y}$ by braking will thus decrease. At the end of the manoeuvre, the top of the area instead corresponds to no braking. Following the manoeuvre along the time evolution, it is seen that the optimal control inputs tend to maximise $F_{c,y}$, except at $t = 0$. It is clear from Figure 6 that to achieve maximum $F_{c,y}$ at the plotted time instants, there is limited room to also perform yaw control by manipulating ΔM .

7. Attainable force volumes during critical manoeuvres

The illustration using attainable force volumes defined by Definition 4.4 in Section 4.3 is used in this section for visualisation of the computed optimal trajectories. The optimal

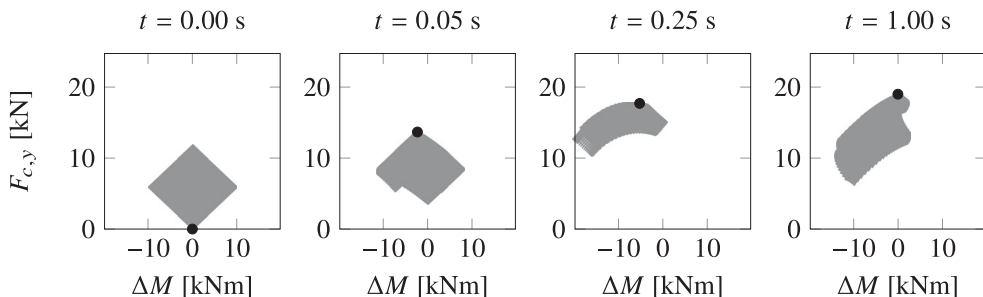


Figure 6. Attainable ΔM and $F_{c,y}$ for the left-hand turn scenario with the optimisation criterion $J = -v_0$. The optimal solution is marked with a black filled circle.

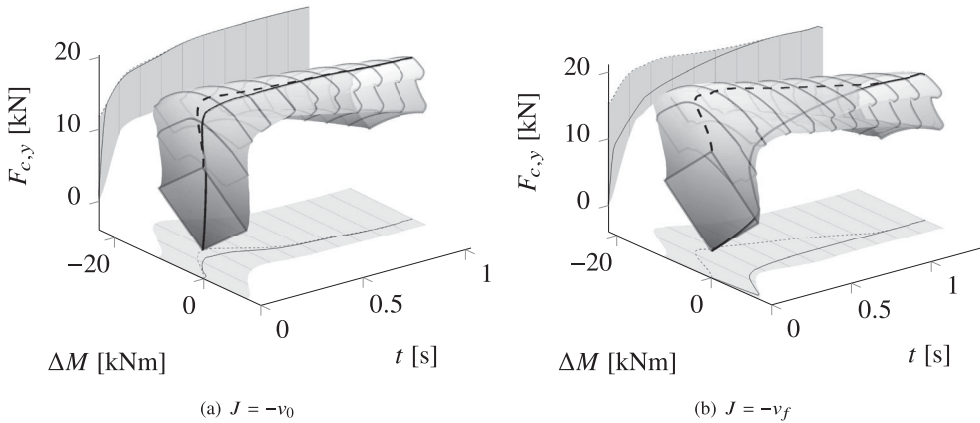


Figure 7. Plots of the attainable force volume $\mathcal{F}(\Delta M, F_{c,y})$ during the left-hand turn scenario for the optimisation criteria $J = -v_0$ and $J = -v_f$. The optimal trajectory is shown as a solid line. The trajectory corresponding to maximum attainable $F_{c,y}$ is shown as a dashed line. Projections are cast on the $F_{c,y}$ and ΔM axes to make it more visible how close the optimal trajectory is to the respective attainable limit.

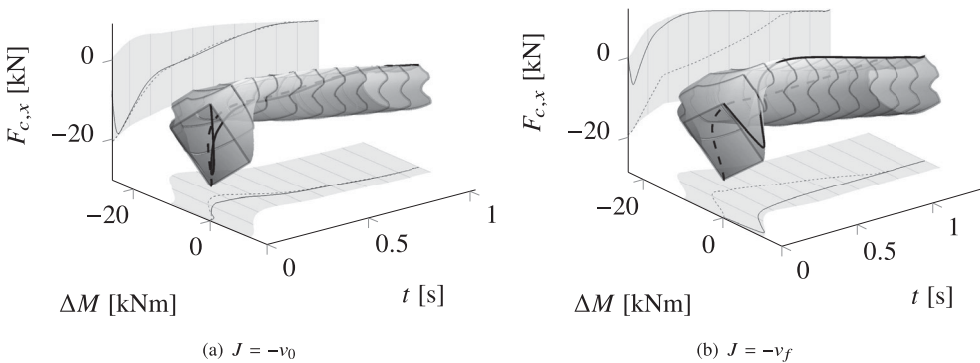


Figure 8. Plots of the attainable force volume $\mathcal{F}(\Delta M, F_{c,x})$ during the left-hand turn scenario for the optimisation criteria $J = -v_0$ and $J = -v_f$, which are the same manoeuvres as in Figure 7. The optimal trajectory is shown as a solid line. The $F_{c,x}$ trajectory corresponding to maximum attainable $F_{c,y}$ is shown as a dashed line. Projections are cast on the $F_{c,x}$ and ΔM axes to make it more visible how close the optimal trajectory is to the respective attainable limit.

trajectory is shown as a solid line traversing in the attainable force volume \mathcal{F} . The trajectory corresponding to the maximum attainable $F_{c,y}$ is shown as a dashed line.

7.1. Left-hand turn

Figures 7 and 8 show the obtained plots of the attainable force volumes $\mathcal{F}(\Delta M, F_{c,y})$ and $\mathcal{F}(\Delta M, F_{c,x})$, respectively. Figure 7(a) visualises the same forces as those presented in Figure 6 and is created from the same optimal solution.

7.1.1. Solutions on the boundary of attainable forces

The forces and moment of the vehicle, F_x , F_y , and M_z , are sometimes considered as high-level inputs in vehicle control systems, but it is challenging to visualise the attainable forces of all three simultaneously, especially if the evolution in time is to be included as an additional dimension. For optimal lane-keeping, it is shown in Section 4.1.2 that for a simplified model, the optimal solution at each time instant is on the boundary of the attainable control force $F_{c,y}$ and moment ΔM . The result of this condition is seen in Figure 7(a), where the optimal trajectory for the optimisation criterion $J = -v_0$ is at or close to the boundary $\partial\mathcal{F}(\Delta M, F_{c,y})$. The same optimal solution is in Figure 8(a) seen to be far from the boundary $\partial\mathcal{F}(\Delta M, F_{c,x})$, except at the end where no braking corresponds to both maximum $F_{c,y}$ and $F_{c,x}$. In the application of optimal lane-keeping here, it is thus possible to reduce the two high-level force inputs F_x and F_y to the single control force $F_{c,y}$, since the optimal trajectory tends to traverse along the boundary $\partial\mathcal{F}(\Delta M, F_{c,y})$. In Figure 7(b), it can be seen that for the optimisation criterion $J = -v_f$, the optimal trajectory is not on $\partial\mathcal{F}(\Delta M, F_{c,y})$ during a majority of the manoeuvre. Instead, this optimal manoeuvre tends to traverse along the boundary $\partial\mathcal{F}(\Delta M, F_{c,x})$ as shown in Figure 8(b).

7.1.2. Moment generation for $J = -v_0$

An interesting observation in Figure 7(a) is that for the optimisation criterion $J = -v_0$, using the braking forces to momentarily maximise the control force $F_{c,y}$ is given priority over a yaw-moment contribution ΔM during the complete manoeuvre. In that case, ΔM takes a value where $F_{c,y}$ is very close to its maximum, not leaving much room for yaw control by differential braking. From this point of view, the turn-out moment contribution from braking that results from the optimisation criterion $J = -v_0$ is intuitive, which is not the case when investigating the trajectories shown in Figure 5. By comparing the optimal trajectory with the trajectory corresponding to maximum attainable $F_{c,y}$ in Figure 7(a), it can be seen that they differ slightly early in the manoeuvre. During this time of the manoeuvre, the top of the boundary $\partial\mathcal{F}(\Delta M, F_{c,y})$ is significantly flat, allowing more turn-in moment to be generated than that given by maximising $F_{c,y}$, at very little loss of $F_{c,y}$.

7.1.3. Initial moment generation for $J = -v_f$

For the optimisation criterion $J = -v_f$, it can be seen in Figure 8(b) that yaw control is initially favored since the yaw moment ΔM is significantly close to its boundary, whereas later $F_{c,x}$ is increasingly given priority. This approach allows the vehicle to more quickly reach higher $F_{c,y}$ by utilising lateral tyre forces, without too much cost in terms of lower $F_{c,x}$. This is interesting as it indicates that traditional stability control systems not only help to reduce run-off-road accidents by keeping the vehicle closer to nominal behaviour and indirectly reducing the velocity, but that the additional turn-in moment from braking generated as a response to understeering is beneficial in itself.

7.1.4. Input-output dynamics

Apart from the very beginning of the manoeuvre for $J = -v_0$ in Figure 7(a), it can be seen that the optimal trajectory is close to the boundary $\partial\mathcal{F}(\Delta M, F_{c,y})$. The wheel dynamics that were neglected in the computation of the attainable forces limit the rate at which the forces can change. Since the other states are relatively slowly changing, it holds for this

manoeuvre that if the limit in terms of the attainable forces has been reached – i.e. if being at the boundary $\partial\mathcal{F}$ – the rate at which the forces can change is fast enough to keep up with the change of the surface of the volume over time.

7.1.5. Direction of resultant force

As observed in Figure 7(a), the solution for $J = -v_0$ is close to maximum attainable $F_{c,y}$ during most parts of the manoeuvre. However, since $F_{c,x}$ is non-zero, it means that the direction of the resultant force does not point exactly in the direction corresponding to the force component $F_{c,y}$, but rather in the direction corresponding to the maximum attainable $F_{c,y}$. This observation is in part the result of the inability to generate an arbitrary lateral force, since the vehicle is limited to front-wheel steering and the steering rate is limited. Since the braking actuators are relatively fast compared to the dynamics of the steering, braking can be used to achieve larger $F_{c,y}$ before the lateral dynamics have caught up, which results in the maximum attainable $F_{c,y}$ from individual braking not coinciding with $F_{c,x} = 0$. Additionally, this observation is also the result of asymmetric tyre forces, i.e. the tyre–road friction coefficients in the longitudinal and lateral directions of the tyres are not equal (the tyre parameters used originate from measured data in [20], where the ratio between the longitudinal and lateral tyre coefficients is 1.25).

7.2. Double lane-change

In this section, the double lane-change scenario is analysed with respect to the attainable force volumes. In order to establish the plot of the attainable force volume $\mathcal{F}(\Delta M, F_{c,y})$ for the double lane-change scenario, the generalised definition of the control force $F_{c,y}$ from Section 4 is used as illustrated in Figure 4. The initial turn toward the left in the double lane-change scenario (see Figure 2) starts at the beginning of the manoeuvre. The final time for the first turn is the time instant when the vehicle is at the closest point along the path to the corner of the first obstacle. At the point where the initial turn ends, the follow-up turn starts. The follow-up turn toward the right ends at the position closest to the top border of the track. In Figure 9, the volume $\mathcal{F}(\Delta M, F_{c,y})$ during the first two turns of the double lane-change scenario is plotted for the optimisation criterion $J = -v_0$.

7.2.1. Moment generation in the initial turn

In Figure 9(a), it is seen that the optimal solution for the initial turn of the double lane-change scenario gives priority to a large $F_{c,y}$, similar to the solution obtained in the left-hand turn scenario investigated in Section 7.1. Compared to the left-hand turn scenario in Figure 7(a), the solution for the initial left-hand turn of the double lane-change scenario does not use the flat section of the boundary $\partial\mathcal{F}(\Delta M, F_{c,y})$ to generate additional turn-in moment from braking, even when it comes at a very small cost in terms of a smaller $F_{c,y}$. Additionally, before the end of the initial turn, the vehicle has already rapidly started to steer in the opposite direction.

7.2.2. Moment generation in the follow-up turn

In the follow-up turn seen in Figure 9(b), the behaviour is different than in the initial turn; here a large focus is on yaw control at the cost of a lower $F_{c,y}$. This observation can be because the follow-up turn has a larger curvature than the initial turn and that the vehicle

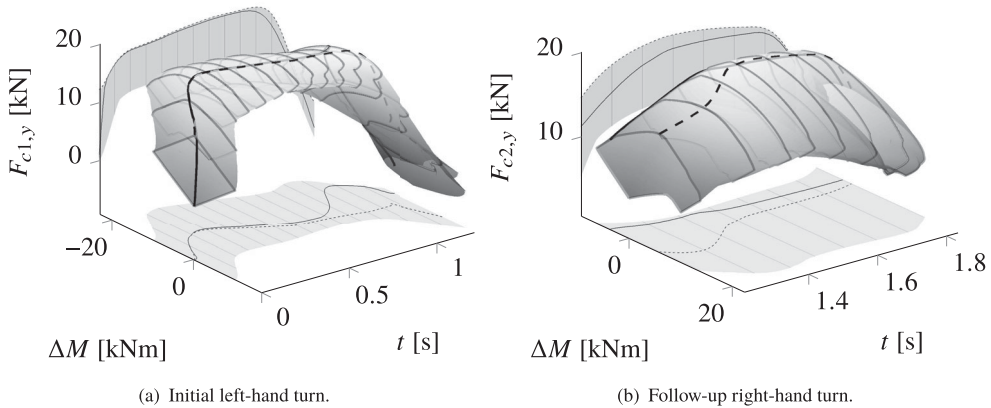


Figure 9. Plots of the attainable force volume $\mathcal{F}(\Delta M, F_{c,y})$ during the double lane-change scenario for the optimisation criterion $J = -v_0$. The first turn of the manoeuvre is shown in the left plot (a) and the follow-up turn in the right plot (b). The direction that $F_{c,y}$ acts in differs between the two turns, as illustrated in Figure 4. The optimal trajectory is shown as a solid line. The trajectory corresponding to maximum attainable $F_{c,y}$ is shown as a dashed line. Projections are cast on the $F_{c,y}$ and ΔM axes to make it more visible how close the optimal trajectory is to the respective attainable limit.

enters the turn from previously turning in the opposite direction, thus having to counteract the inertia. Yaw control can thus play a significant role also in lane-keeping control to keep the vehicle on the road.

7.2.3. Solutions on the boundary of attainable forces

The same behaviour as observed for the left-hand turn in Section 7.1.1 is seen in Figure 9 for the double lane-change manoeuvre, where the solution is typically on the boundary $\partial\mathcal{F}(\Delta M, F_{c,y})$. The exception is from the middle point of the follow-up turn until close to the end, where the optimal trajectory is a notable distance from the boundary $\partial\mathcal{F}(\Delta M, F_{c2,y})$. In this time interval, the velocity is low as a result of braking (≈ 30 km/h). A likely reason is that the braking actuators are not fast enough to stay at the boundary $\partial\mathcal{F}(\Delta M, F_{c2,y})$ because of rapid changes in the vehicle yaw rate and orientation. These limitations mean that contrary to what is described in Section 7.1.4 for the left-hand turn, the rate at which the tyre forces has to change is too fast during the follow-up turn for the optimal trajectory to stay at the surface of the attainable force volume.

8. Global forces for controller design

An interesting aspect is to use the results obtained from the analysis of the attainable force volumes in autonomous functions for control and safety in future road vehicles. Ideally, the analysis of optimal vehicle manoeuvres can give inspiration for, and even lead to the development of new improved autonomous functions. The analytical motivation in Section 4.1.2 and the numerical results observed in Section 7.1.1 and Section 7.2.3, indicate that for a given geometry and vehicle state, a local control approach to find an appropriate solution on the boundary $\partial\mathcal{F}$ in fact converges toward the globally optimal

solution. This observation holds promise for improved lane-keeping control designs based on maximising a global force in the spirit of [4,12,16,18,31,32].

For such a control function to be applicable in online scenarios, the desired global force needs to be possible to compute fast, given information about the traffic situation and the environment. Assuming the availability of such information, the control task is firstly to compute the direction that the global force on the vehicle should act in and secondly to actuate the vehicle such that the acceleration of the vehicle is maximised in the desired direction. In such a control design, attainable force volumes as introduced in Section 4, and illustrated with extensive results for different optimal braking and steering manoeuvres in Section 7, can play an important role in the development. More specifically, the observed results can be employed to analyse the vehicle forces during optimal vehicle manoeuvres as a comparison with theoretically attainable force–moment relations. In addition, the plots of attainable force volumes are a useful tool for evaluation of the resulting forces from a particular control design for an autonomous function, since the global forces and moments can be plotted in the volume and then be used to evaluate how the tyre forces are utilised.

An online estimation of the desired global force can be performed by using analytical solutions from optimal control based on a friction-limited particle model. This approach was used in [4], where a road-departure prevention system was developed for the left-hand turn scenario. For optimal control of a friction-limited particle model, the solution is given on the circular force boundary given by the friction limit and what remains is to solve for which direction the force vector should point in. This can be interpreted as it being important to control the direction of the force vector, but as observed for optimal control of the more complex model in Section 4.1.2, the more general interpretation is that the force component in this direction should be maximised. Further support is given by the numerical solutions analysed in Section 7.1.5, where it was noted that while close-to-maximum $F_{c,y}$ was obtained during optimal lane-keeping, $F_{c,x}$ was non-zero. This observation has implications for the implementation and evaluation of lane-keeping systems, and still applies for a vehicle with isotropic tyre-friction coefficients, owing to differences in longitudinal and lateral tyre-force dynamics as a result of actuator limitations.

9. Conclusions

For the development of optimal lane-keeping control systems, it is critical to understand how the available tyre forces can be used in the best possible way. The research presented here is an extension of previous research for a friction-limited particle model to a more complex model and further scenarios. To extend that research, a number of important global forces and moments were defined, and the new concept of attainable force volumes was introduced. A specific finding is that for lane-keeping it is important to maximise the force in a certain direction, rather than to control the direction of the force vector, even though these two strategies are equivalent for a friction-limited particle model. To support the findings, an analytical argument based on the maximum principle was presented. Under slight simplifications it was shown that the optimal behaviour develops on the boundary surface of the attainable force volume. This was further supported by numerical solutions to optimal control problems in different scenarios. Here, attainable force volumes were introduced and turned out to provide an effective illustration of how the achieved trajectory relates to the attainable forces over the duration of the manoeuvre.

Another finding from this analysis was that for optimal lane keeping in both the left-hand turn scenario and the initial turn of the double lane-change scenario, $F_{c,y}$ is close to its maximum attainable value. Further, when comparing the optimal trajectory with the trajectory corresponding to maximum attainable $F_{c,y}$ for these cases, it is observed that they are very close. These findings indicate that there are some manoeuvres requiring combined braking and steering where close to optimal behaviour can be found by at each time instant maximising $F_{c,y}$, leading to simplified control design. Applied to lane-keeping control, the results indicate a set of control principles for autonomous at-the-limit manoeuvres, which can be implemented and executed online. This set contains strategies similar to those analytically obtained for friction-limited particle models in previous research, but was shown to result in vehicle behaviour close to the globally optimal solution also for more complex models and scenarios.

Disclosure statement

No potential conflict of interest was reported by the authors.

Funding

The authors are members of the ELLIIT Excellence Center, the Strategic Area for ICT research, supported by the Swedish Government. This work was partially supported by the Wallenberg AI, Autonomous Systems and Software Program (WASP) funded by the Knut and Alice Wallenberg Foundation.

ORCID

Victor Fors  <http://orcid.org/0000-0003-4034-2868>

Björn Olofsson  <http://orcid.org/0000-0003-1320-032X>

References

- [1] Lundahl K, Olofsson B, Berntorp K, et al. Towards lane-keeping electronic stability control for road-vehicles. In: Proceedings of the 19th IFAC World Congress. Cape Town, South Africa; 2014. p. 6319–6325.
- [2] Fors V, Olofsson B, Nielsen L. Formulation and interpretation of optimal braking and steering patterns towards autonomous safety-critical manoeuvres. *Veh Syst Dyn*. 2018. doi:10.1080/00423114.2018.1549331.
- [3] Klomp M, Lidberg M, Gordon TJ. On optimal recovery from terminal understeer. *Proc Inst Mech Eng Part D J Automob Eng*. 2014;228(4):412–425.
- [4] Gao Y, Gordon TJ, Lidberg M, et al. An autonomous safety system for road departure prevention based on combined path and sideslip control. In: *The Dynamics of Vehicles on Roads and Tracks – Proceedings of the 24th Symposium of the International Association for Vehicle System Dynamics (IAVSD2015)*. Graz, Austria: 2016. p. 281–286.
- [5] Falcone P, Borrelli F, Tseng HE, et al. Linear time-varying model predictive control and its application to active steering systems: stability analysis and experimental validation. *Int J Robust Nonlinear Control*. 2008;18(8):862–875.
- [6] Beal CE, Gerdes JC. Model predictive control for vehicle stabilization at the limits of handling. *IEEE Trans Control Syst Technol*. 2013 Jul;21(4):1258–1269.
- [7] Brown M, Funke J, Erlien S, et al. Safe driving envelopes for path tracking in autonomous vehicles. *Control Eng Pract*. 2017;61:307–316.
- [8] Kritayakirana K, Gerdes JC. Autonomous vehicle control at the limits of handling. *Int J Veh Auton Syst*. 2012;10(4):271–296.

- [9] Ni J, Hu J. Dynamics control of autonomous vehicle at driving limits and experiment on an autonomous formula racing car. *Mech Syst Signal Process.* 2017;90:154–174.
- [10] Laurence VA, Gerdes JC. Speed control for robust path-tracking for automated vehicles at the tire–road friction limit. In: 14th International Symposium on Advanced Vehicle Control (AVEC). Beijing, China; 2018.
- [11] Jonasson M, Andreasson J, Jacobson B. Global force potential of over-actuated vehicles. *Veh Syst Dyn.* 2010;48(9):983–998.
- [12] Gao Y, Lidberg M, Gordon TJ. Modified Hamiltonian algorithm for optimal lane change with application to collision avoidance. *MM Sci J.* 2015 Mar;2015:576–584.
- [13] Sundström P, Jonasson M, Andreasson J, et al. Path and control signal optimisation for over-actuated vehicles in two safety-critical maneuvers. In: 10th International Symposium on Advanced Vehicle Control (AVEC10). Loughborough, UK; 2010.
- [14] Smith EN, Velenis E, Tavernini D, et al. Effect of handling characteristics on minimum time cornering with torque vectoring. *Veh Syst Dyn.* 2017;56(2):221–248.
- [15] Yang D, Gordon TJ, Jacobson B, et al. Optimized brake-based control of path lateral deviation for mitigation of secondary collisions. *Proc Inst Mech Eng Part D J Automob Eng.* 2011;225(12):1587–1604.
- [16] Yang D, Gordon TJ, Jacobson B, et al. Quasi-linear optimal path controller applied to post impact vehicle dynamics. *IEEE Trans Intell Transp Syst.* 2012;13(4):1586–1598.
- [17] Yang D, Jacobson B, Jonasson M, et al. Minimizing vehicle post impact path lateral deviation using optimized braking and steering sequences. *Int J Automot Technol.* 2014 Feb;15(1):7–17.
- [18] Yang D, Jacobson B, Jonasson M, et al. Closed-loop controller for post-impact vehicle dynamics using individual wheel braking and front axle steering. *Int J Veh Auton Syst.* 2014;12(2):158–179.
- [19] ISO 3888-2:2011. Passenger cars – test track for a severe lane-change manoeuvre – Part 2: obstacle avoidance. International Organization for Standardization (ISO). Geneva, Switzerland. 2011.
- [20] Pacejka HB. Tyre and vehicle dynamics. 2nd ed. Oxford: Butterworth-Heinemann; 2006.
- [21] Berntorp K, Olofsson B, Lundahl K, et al. Models and methodology for optimal trajectory generation in safety-critical road–vehicle manoeuvres. *Veh Syst Dyn.* 2014;52(10):1304–1332.
- [22] Åkesson J, Årzén KE, Gäfvert M, et al. Modeling and optimization with Optimica and JModelica.org – Languages and tools for solving large-scale dynamic optimization problems. *Comput Chem Eng.* 2010;34(11):1737–1749.
- [23] Biegler LT, Cervantes AM, Wächter A. Advances in simultaneous strategies for dynamic process optimization. *Chem Eng Sci.* 2002;57(4):575–593.
- [24] Wächter A, Biegler LT. On the implementation of an interior-point filter line-search algorithm for large-scale nonlinear programming. *Math Program.* 2006;106(1):25–57.
- [25] HSL. A collection of Fortran codes for large scale scientific computation. 2017; [cited 2017 Feb 15]. Available from: <http://www.hsl.rl.ac.uk/>
- [26] Andersson JAE, Gillis J, Horn G, et al. CasADi – A software framework for nonlinear optimization and optimal control. *Math Program Comput.* 2019;11(1):1–36.
- [27] Peters SC. Optimal planning and control for hazard avoidance of front-wheel steered ground vehicles [dissertation]. Massachusetts Institute of Technology; 2012.
- [28] Shiller Z, Sundar S. Emergency lane-change maneuvers of autonomous vehicles. *ASME J Dyn Syst Meas Control.* 1998;120(1):37–44.
- [29] Neustadt LW, Pontryagin L. The mathematical theory of optimal processes. New York: Interscience; 1965. (1962)
- [30] Glad T, Ljung L. Control theory. London: Taylor & Francis; 2000.
- [31] Fors V, Olofsson B, Nielsen L. Slip-angle feedback control for autonomous safety-critical maneuvers at-the-limit of friction. In: 14th International Symposium on Advanced Vehicle Control (AVEC18). Beijing, China; 2018.
- [32] Arikere A, Yang D, Klomp M. Optimal motion control for collision avoidance at Left Turn Across Path/Opposite Direction intersection scenarios using electric propulsion. *Veh Syst Dyn.* 2019;57(5):637–664.